Electronic Supplementary Material (ESI) for Soft Matter.

Dark-field differential dynamic microscopy: Electronic supplementary information

Alexandra V. Bayles, Todd M. Squires, and Matthew E. Helgeson*

Department of Chemical Engineering, University of California Santa Barbara, 3357 Engineering II, Santa Barbara, CA 93106, USA. Fax: +1-(805)-893-4731; Tel: +1-(805)-893-3372; E-mail: helgeson@engineering.ucsb.edu

1 Intensity profile additivity

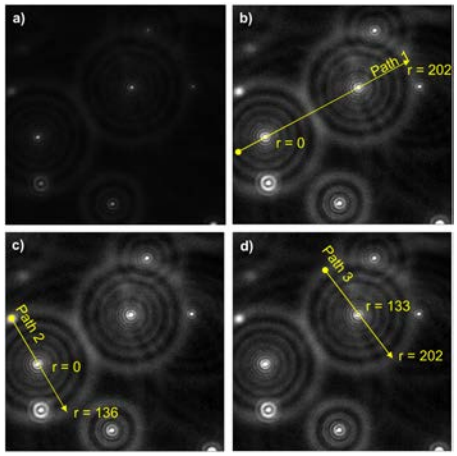

Figure S1 Dark-field micrographs of Au nanoparticles that have overlapping intensity profiles. A) Original dark-field micrograph. B) Contrast enhanced micrograph makes the overlapping rings of the intensity profiles more obvious. Path 1 is in a direction where the intensity profiles of the two relatively close intensity profiles overlap. Paths 2 and 3 pictured in c) and d) are approximately perpendicular to Path 1. Values of r correspond to those in Figure S2.

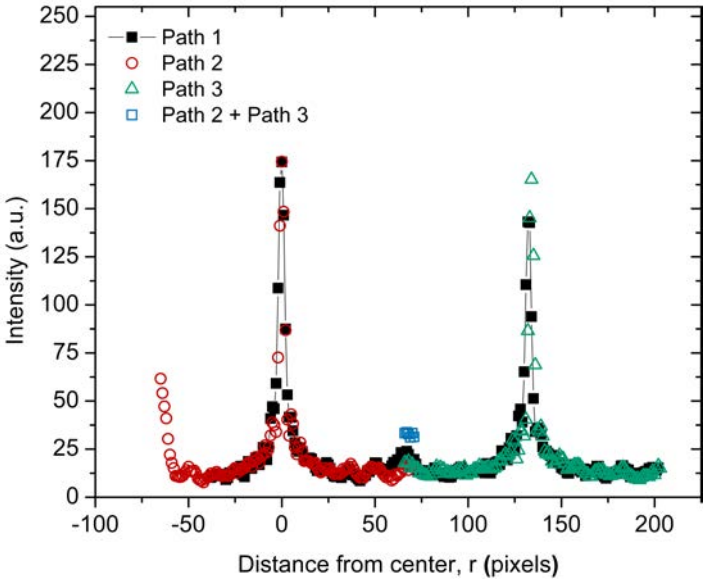

Figure S2 Values of the intensity profiles across the paths shown in Figure S1. Adding Paths 2 and 3 across the intersection shows that the rings in the intensity profile are roughly additive. The difference between the sum of the two paths and the recorded value is 8.8 intensity units, which is 37% of the recorded value at the intersection, and 5% of the value of the maximum intensity of the main peaks which are the principal contributors to the image structure function.

2 Sucrose solution viscosities

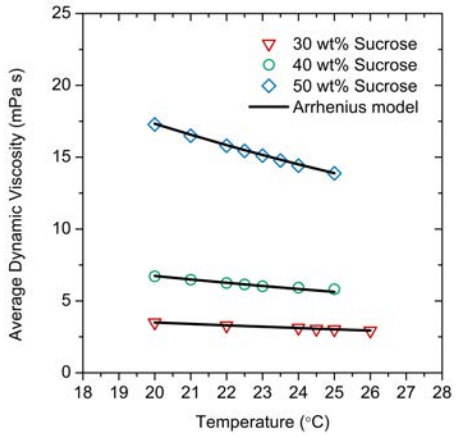

Figure S3 Temperature dependence of sucrose solution viscosities. Error bars smaller than markers.

3 Additional information on image structure function fitting

Micrograph videos were processed using a DDM analysis algorithm written and executed in MATLAB. Each video was first separated into individual frames. Frames separated by time step Δt were subtracted from one another, and the resulting difference image was fast Fourier transformed. In $\mathbf{q} = (q_x, q_y)$ space, the transformed intensity was radially averaged with $q = (q_x^2 + q_y^2)^{1/2}$. The ensemble average was taken over all frames separated by Δt, giving $D(q, \Delta t)$. At minimum, 100 image differences contributed to each average to ensure adequate statistics.

For each q value, $D(q, \Delta t)$ was fit to

$$D(\Delta t) = A\left[1 - e^{-\Delta t \Gamma}\right] + B \tag{1}$$

using MATLAB's nonlinear curve fitting function, *lsqcurvfit*. A, B and Γ are fitting parameters that vary with each isowavevector (note that $\Gamma = \tau^{-1}$). Using the *lsqcurvfit* algorithm, the user has the option to specify (1) the fitting algorithm (here, we used the trust-region reflective algorithm) and (2) to specify initial values and upper and lower bounds on the three parameters A, B and Γ to improve convergence toward physically reasonable fits in a shorter amount of time. Since $D(q, \Delta t)$ spans multiple orders of magnitude, the isowavevectors were divided into 4 ranges, each of which had different bounds and initial guesses for the fit parameters. The q ranges and corresponding initial values and bounds are listed for the 10× and 40× videos in Tables S1 and S2 respectively. The A and Γ bounds were intentionally made to be orders of magnitude larger than the values identified in the final fits so as to prevent biasing toward local fit minima. The constraints placed on $B(q)$ were such that the fit values obtained for $A(q)$ and $\Gamma(q)$ were within their constrained ranges. In some cases, this produces vanishingly small values of $B(q)$ (i.e. $B(q)$ is statistically indistinguishable from zero). Bounds and initial values could be found for B if a faster camera was used to sample the plateau in $B(q)$ at short times, as done by He *et al.*[16] Despite the limited frame rate of the camera, we still obtain fits that agree well with the MPT diffusivities using this fitting procedure.

Fits with R^2 correlation values less than 95% were excluded from further analysis of $\tau(q)$ to eliminate cases where eqn (6) did not fit the empirical $D(\Delta t)$. Fits that were rejected were nearly exclusively in regions of low q (typically $q < 0.2\,\mu m^{-1}$) where the video was too short for the image structure function to reach an appreciable long-time plateau, and in regions of high q (typically $q > 3\,\mu m^{-1}$) where the frame rate was too slow to measure dynamics.

Table S1 DDM fit parameter bounds and initial values for micrograph videos recorded at 10×

q range (μm^{-1})	Γ bounds (s^{-1})	Γ initial (s^{-1})	A bounds (a.u.)	A initial	B bounds (a.u.)	B initial
$0.019 < q \leq 1.180$	$0 \leq \Gamma \leq D_{selfguess} * 1.180^2 + 100$	$D_{selfguess} * 1.180^2$	$10 \leq A \leq 10^6$	10^3	$0 \leq B \leq 0.25$	0.1
$1.180 < q \leq 2.398$	$0 \leq \Gamma \leq D_{selfguess} * 2.398^2 + 100$	$D_{selfguess} * 2.398^2$	$10 \leq A \leq 10^5$	10^2	$0 \leq B \leq 0.25$	0.1
$2.398 < q \leq 3.616$	$0 \leq \Gamma \leq D_{selfguess} * 3.616^2 + 100$	$D_{selfguess} * 3.616^2$	$0 \leq A \leq 10^5$	10^2	$0 \leq B \leq 0.25$	0.1
$3.616 < q \leq 4.851$	$0 \leq \Gamma \leq D_{selfguess} * 4.851^2 + 100$	$D_{selfguess} * 4.851^2$	$0 \leq A \leq 10^5$	0	$0 \leq B \leq 0.25$	0.1

Note: $D_{selfguess}$ was $0.4\mu m^2/s$, $0.8\mu m^2/s$, and $1.5\ \mu m^2/s$ for the 30 *wt%*, 40 *wt%* and 50 *wt%* sucrose solutions respectively.

Table S2 DDM fit parameter bounds and initial values for micrograph videos recorded at 40×

q range (μm^{-1})	Γ bounds (s^{-1})	Γ initial (s^{-1})	A bounds (a.u.)	A initial	B bounds (a.u.)	B initial
$0.076 < q \leq 4.729$	$0 \leq \Gamma \leq D_{selfguess} * 4.729^2 + 100$	$D_{selfguess} * 4.729^2$	$10 \leq A \leq 10^6$	10^3	$0 \leq B \leq 0.25$	0.1
$4.729 < q \leq 9.611$	$0 \leq \Gamma \leq D_{selfguess} * 9.611^2 + 100$	$D_{selfguess} * 9.611^2$	$10 \leq A \leq 10^5$	10^2	$0 \leq B \leq 0.25$	0.1
$9.611 < q \leq 14.493$	$0 \leq \Gamma \leq D_{selfguess} * 14.493^2 + 100$	$D_{selfguess} * 14.493^2$	$0 \leq A \leq 10^5$	10^2	$0 \leq B \leq 0.25$	0.1
$14.493 < q \leq 19.451$	$0 \leq \Gamma \leq D_{selfguess} * 19.451^2 + 100$	$D_{selfguess} * 19.451^2$	$0 \leq A \leq 10^5$	0	$0 \leq B \leq 0.25$	0.1

Note: $D_{selfguess}$ was $0.4\mu m^2/s$, $0.8\mu m^2/s$, and 1.5 $\mu m^2/s$ for the 30 *wt%*, 40 *wt%* and 50 *wt%* sucrose solutions respectively.

4 Additional LSV simulations

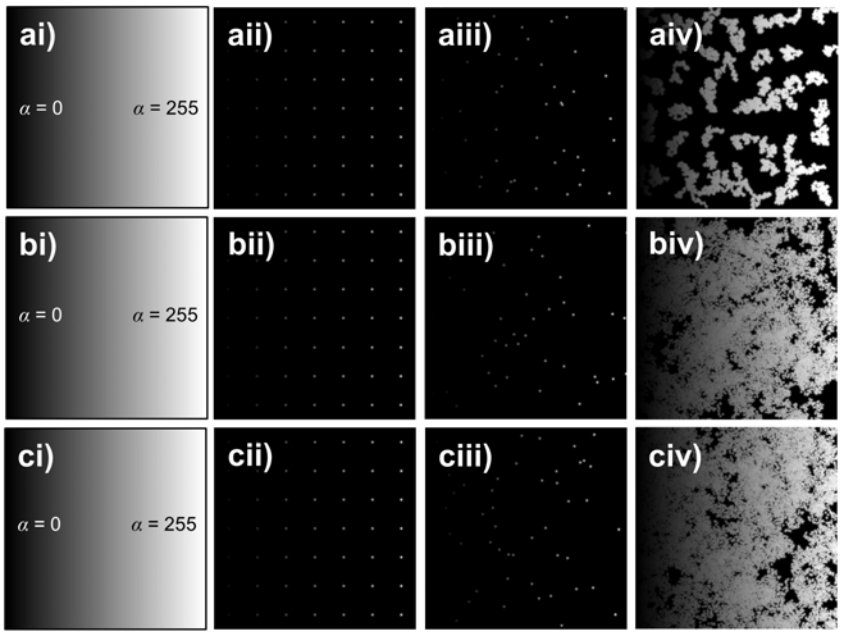

Figure S4 Brownian motion simulations in physically reasonable LSV imaging system for long times. Rows correspond to three different simulations that take place in the same linear gradient illumination system where $\chi = 5 \times 10^{-3}$. a) is the same simulation described in Fig. 5b); it has a total length of 900 frames. b) is a simulation that takes place over the time equivalent of 9000 frames where no boundary conditions are applied c) is a simulation that takes place over the time equivalent of 9000 frames where periodic boundary conditions are imposed in the vertical direction and mirror boundary conditions are imposed in the horizontal direction. Columns correspond to different aspects of the simulations. i) Spatial dependence of the magnitude of particle intensity, α. ii) Micrograph of 49 particles initialized on a square lattice at t = 0. iii) Micrograph at t = 800 frames in simulation a) and t = 8000 frames for simulation b) and c). Close examination at this time step shows that N = 49 in simulation (a); N = 43 in simulation (b); and N = 49 in simulation (c). iii) Particle trajectories after the full duration of the micrograph series.

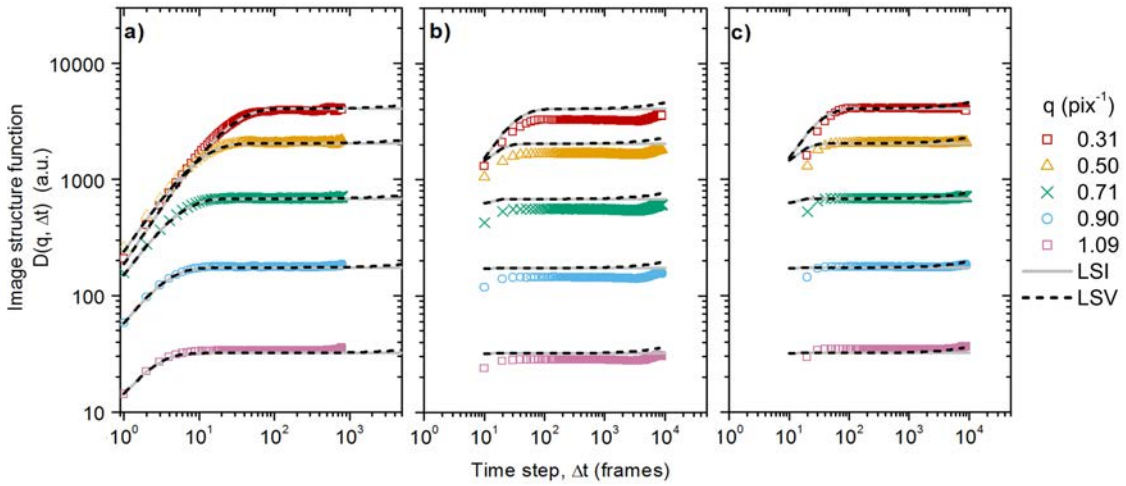

Figure S5 Analyzing the image structure function of long time simulated micrographs. The calculated image structure functions in a), b), and c) correspond to simulations a), b), and c) in Fig. S4. Dashed and solid lines correspond to the analytical LSV (eqn (41)) and LSI (eqn (40)) functions for Gaussian particles respectively. As discussed in the main text, both the LSI and LSV analytical expressions fit $D(q,\Delta t)$ in simulation (a) agree well over the time period required to extract diffusivity. In the longer simulation (b), differences appear between values of $D(q,\Delta t)$ predicted by eqns (41) and (40) for LSV and LSI systems, respectively. Values of $D(q,\Delta t)$ "measured" from simulations in LSV systems deviate from the LSI predictions on the time scale predicted by the LSV theory, and the height of the upturn relative to the uncorrelated plateau is predicted by the theory. However, both the LSI and LSV theory quantitatively overestimate the uncorrelated plateau because the particles are allowed to diffuse their true displacement out of the micrograph space. This causes the simulation to on average have fewer than 49 particles per frame. $A(q)$, which primarily determines the magnitude of the uncorrelated plateau, is directly proportional to the number of particles N. Consequently, when there are fewer particles in the frame, both theories overestimate the long term plateau. The issue of particles diffusing out of frame can be reconciled by imposing periodic and mirror boundary conditions on the simulation, as done in simulation (c). Imposing the BCs corrects the plateau overestimation, but also introduces additional artifacts, including unreasonably small displacements near the edge of the boundary which weakens the increase in the image structure function at long times.

5 Additional information on experimental dark-field DDM

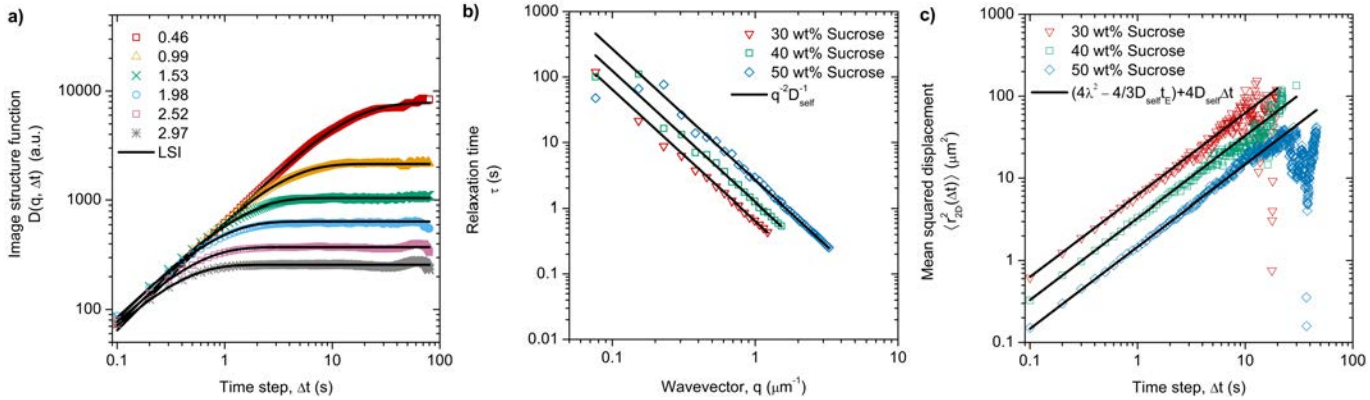

Figure S6 Measuring nanoparticle diffusivity via dark-field DDM and multiple particle tracking. a) Image structure function of 100 nm Au nanoparticles in 50 wt% sucrose solution imaged under dark-field microscopy (40× magnification). Experimental image structure function fits well to the linear space invariant decomposition, eqn (2), due to the low value of χ in the experimental system. b) Relaxation time $\tau(q)$ as a function of wavevector q for 100 nm Au NP sucrose dispersions. c) Mean squared displacements of tracked 100 nm Au NPs. Noise in $< r_{2D}^2(\Delta t) >$ at large Δt is due to the smaller number of trajectories that contribute to the average.

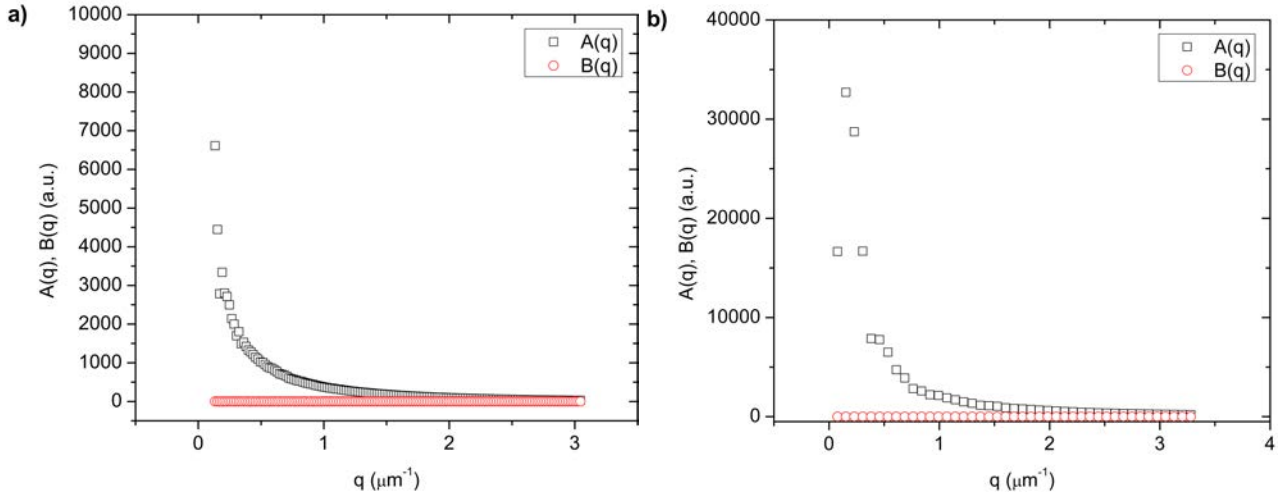

Figure S7 Representative plots of $A(q)$ and $B(q)$ obtained during fitting of the image structure function. a) $A(q)$ and $B(q)$ obtained from the image structure function of 100 nm Au nanoparticles in 30 wt% sucrose solution imaged under dark-field microscopy at 10× magnification (see Fig. 1d for the corresponding image structure function). b) $A(q)$ and $B(q)$ obtained from the image structure function of 100 nm Au nanoparticles in 50 wt% sucrose solution imaged under dark-field microscopy at 40× magnification (see Fig. S6a for the corresponding image structure function).